Unveiling the high-activity origin of single-atom iron catalysts for oxygen reduction reaction

Liu Yang[a,b,1], Daojian Cheng[a,b,1], Haoxiang Xu[a,b], Xiaofei Zeng[a,b], Xin Wan[c], Jianglan Shui[c], Zhonghua Xiang[a,b], and Dapeng Cao[a,b,2]

[a]Beijing Advanced Innovation Center for Soft Matter Science and Engineering, Beijing University of Chemical Technology, 100029 Beijing, People's Republic of China; [b]State Key Laboratory of Organic-Inorganic Composites, Beijing University of Chemical Technology, 100029 Beijing, People's Republic of China; and [c]School of Materials Science and Engineering, Beihang University, 100083 Beijing, People's Republic of China

Edited by Alexis T. Bell, University of California, Berkeley, CA, and approved May 16, 2018 (received for review January 14, 2018)

It is still a grand challenge to develop a highly efficient nonprecious-metal electrocatalyst to replace the Pt-based catalysts for oxygen reduction reaction (ORR). Here, we propose a surfactant-assisted method to synthesize single-atom iron catalysts (SA-Fe/NG). The half-wave potential of SA-Fe/NG is only 30 mV less than 20% Pt/C in acidic medium, while it is 30 mV superior to 20% Pt/C in alkaline medium. Moreover, SA-Fe/NG shows extremely high stability with only 12 mV and 15 mV negative shifts after 5,000 cycles in acidic and alkaline media, respectively. Impressively, the SA-Fe/NG-based acidic proton exchange membrane fuel cell (PEMFC) exhibits a high power density of 823 mW cm^{-2}. Combining experimental results and density-functional theory (DFT) calculations, we further reveal that the origin of high-ORR activity of SA-Fe/NG is from the Fe-pyrrolic-N species, because such molecular incorporation is the key, leading to the active site increase in an order of magnitude which successfully clarifies the bottleneck puzzle of why a small amount of iron in the SA-Fe catalysts can exhibit extremely superior ORR activity.

single-atomic iron catalysts | oxygen reduction reaction | Fe-pyrrolic-N moieties | N-doped porous carbons | density-functional theory

To meet the clean energy requirements in the future, the acidic proton exchange membrane fuel cell (PEMFC) and rechargeable metal–air battery with high energy densities have been considered as the most promising vehicle power suppliers (1). The oxygen reduction reaction (ORR) plays a key role in the PEMFC and metal–air battery, because the rate of ORR in cathode is several orders slower than hydrogen oxidation reaction in anode and they severely rely on the precious Pt-based catalysts, which extremely hinders their commercial applications (2, 3). Therefore, development of highly active nonprecious metal ORR catalysts is of significant importance to boost their applications (4, 5).

Previous investigations indicate that the iron and nitrogen-codoped porous carbons are one of the most promising ORR catalysts (6, 7). Currently, the ORR performance of most Fe-N-C catalysts exceeds commercial 20% Pt/C in alkaline conditions but are still less by about 60 mV than Pt/C in acidic conditions (2, 3, 5, 8), which is attributed to the different states of the active sites in acidic and alkaline conditions (9). Unfortunately, there are still many difficulties in the design of refined metal-N-C configuration since the transitional-metal–containing precursors can easily turn into uncontrollable metal clusters at a high temperature, leading to a relatively weak catalytic activity and hindering the profound understanding of the active sites (10). Compared with metal-clusters–doped catalysts, metallic single-atom catalysts (SACs) provide the maximum atomic efficiency, and possess the refined M-N-C configuration (M = Fe, Co, and Ni, etc.) and the strong interaction between single atom (SA) and supports, which offers an ideal model to develop the highly efficient catalysts and further explore the origin of high catalytic activity (11–15). Most recently, several research groups have successfully synthesized SACs and the configurations of the active sites were determined by the precise characterization (6, 12, 16–28). However, the origin of high ORR activity of SACs is indefinite, and the effect of the coordination of single-atom and the different N species on the ORR activity is yet unclear (29, 30). Therefore, revealing the origin of high-ORR activity of SACs is extremely significant for development of highly efficient catalysts.

Here we report a surfactant-assisted method to synthesize the SA Fe catalysts supported on nitrogen-doped graphitic carbons (marked as SA-Fe/NG). SA-Fe/NG exhibits extremely outstanding ORR activities in acidic and alkaline media. Moreover, the SA-Fe/NG-based acidic PEMFC exhibits a high power density of 823 mW cm^{-2}, which indicates that SA-Fe/NG is among the rank of excellent nonprecious-metal ORR catalysts. By combining experimental results and density-functional theory (DFT) calculations, we further reveal that the origin of high-ORR activity of SA-Fe catalysts is from the Fe-pyrrolic-N species, because such molecular incorporation leads to the increase of active sites in an order of magnitude, i.e., creating an Fe atom and eight C atom active sites next to pyrrolic N, which opens an approach for developing not only the excellent ORR catalysts but also other heterogeneous catalysts.

Results and Discussion

The surfactant-assisted synthesis process of the SA-Fe/NG is shown in Fig. 1*A*, in which the SA-Fe/NG sample can be obtained by pyrolyzing the layered-like precursor formed by Fe-loaded F127 [F127 is a water-soluble surfactant of polyoxyethylene–polyoxypropylene–polyoxyethylene (PEO-PPO-PEO)] and g-C_3N_4 (Fig. 1*A* and *SI Appendix*, Fig. S1). To highlight the importance of surfactant in the synthesis, Fe/NG sample was also prepared by the same process but without the addition of surfactant F127.

Significance

We propose a surfactant-assisted method to synthesize single-atom iron catalysts (SA-Fe/NG) supported on nitrogen-doped graphitic carbons, and experimentally demonstrated that the SA-Fe/NG catalyst possesses extremely outstanding catalytic activities for oxygen reduction reaction (ORR) in both acidic and alkaline media. Impressively, both the SA-Fe/NG-based acidic proton exchange membrane fuel cell and Zn-air battery show excellent performance. Combining experimental results and density-functional calculations, we reveal that the origin of high-ORR activity of SA-Fe/NG is from the Fe-pyrrolic-N_4 active species. The universal surfactant-assisted method can be easily extended to synthesis of other single-atom catalysts, and unveiling the origin of high-ORR activity of SA-Fe/NG will open an approach for developing other heterogeneous catalysts.

Author contributions: D. Cao designed research; L.Y., D. Cheng, H.X., X.W., J.S., and D. Cao performed research; L.Y., X.Z., Z.X., and D. Cao analyzed data; and L.Y. and D. Cao wrote the paper.

The authors declare no conflict of interest.

This article is a PNAS Direct Submission.

[1]L.Y. and D. Cheng contributed equally to this work.

[2]To whom correspondence should be addressed. Email: caodp@mail.buct.edu.cn.

This article contains supporting information online at www.pnas.org/lookup/suppl/doi:10.1073/pnas.1800771115/-/DCSupplemental.

Published online June 11, 2018.

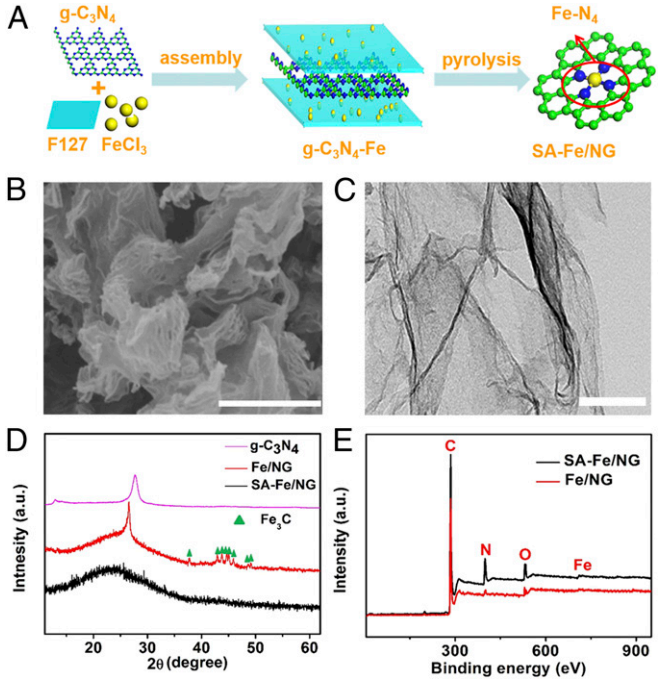

Fig. 1. Synthesis illustrations and characterizations of SA-Fe/NG. (*A*) Schematic procedure for the synthesis of SA-Fe/NG catalyst. (*B*) SEM image (scale bar, 200 nm) and (*C*) TEM image of SA-Fe/NG (scale bar, 200 nm) of SA-Fe/NG. (*D*) PXRD graphs of g-C_3N_4, SA-Fe/NG and Fe/NG. (*E*) XPS spectra of SA-Fe/NG and Fe/NG samples.

The SEM and transmission electron microscopy (TEM) images (Fig. 1 *B* and *C*) show that SA-Fe/NG is the graphene-like structure without Fe aggregation, which is also verified by powder X-ray diffraction (PXRD) (Fig. 1*D*), where SA-Fe/NG shows only one broad carbon peak at ∼26°and no other sharp peaks of crystalline metallic Fe and/or Fe compounds. The importance of F127 might be related to the extension of surface area and therefore less agglomeration (and carbide formation), which may be the origin of larger site density of samples. However, the elemental mapping (*SI Appendix*, Fig. S2) and X-ray photoelectron spectroscopy (XPS) (Fig. 1*E* and *SI Appendix*, Table S1) exhibit the presence of Fe element in SA-Fe/NG, which means that Fe may be atomically dispersed on N-doped graphitic carbons. The high-resolution Fe 2p spectrum of SA-Fe/NG shows two peaks at 710.8, 713.7, 719.3, and 724 eV corresponding to Fe $2p_{2/3}$ and Fe $2p_{1/2}$ (*SI Appendix*, Fig. S3*A*) (31), and no peak between 700 and 710 eV is assigned to zero-valence iron, indicating that the iron atom is mostly coordinated with the surrounding nitrogen atoms. However, without surfactant addition, Fe/NG exhibits well-defined diffraction peaks associated with Fe-based carbides (Fig. 1*D* and *SI Appendix*, Fig. S4), where these Fe-based carbide clusters cannot be etched by acid (19). The high-resolution N 1s spectrum (*SI Appendix*, Fig. S3*B*) can be fitted into three peaks at 398.4, 400.1, and 401.0 eV, corresponding to pyridinic N, pyrrolic N/Fe-N, and quaternary N, respectively (32). The XPS data indicate that the contents of total nitrogen and pyrrolic N/Fe-N of SA-Fe/NG are greatly higher than Fe/NG (*SI Appendix*, Figs. S3*B* and S5 and Table S1). The possible reason is that the addition of F127 effectively prevents the loss of nitrogen, due to the formation of Fe-loaded F127 nanosheet by the electrostatic interaction. Moreover, SA-Fe/NG possesses apparently larger Brunauer–Emmett–Teller-specific surface area and pore volume than Fe/NG (*SI Appendix*, Fig. S6 and Table S2). Obviously, the surfactant-assisted synthetic strategy is an effective and facile method to prepare SACs, because the Fe-doped surfactant F127 sheets tightly anchor on g-C_3N_4 substrate so that the Fe can easily coordinate with nitrogen in the pyrolysis process. Meanwhile, the Fe clusters formed on the surface can be easily removed by pickling (*SI Appendix*, Figs S7 and S8) (33).

The high-angle annular dark-field scanning TEM (HAADF-STEM) image of SA-Fe/NG (Fig. 2*A*) exhibits many evenly scattered bright spots at an atomic scale. The spots are assigned to the iron atom, which was further confirmed by electron energy loss spectroscopy (EELS, Fig. 2*B*). The selected area in Fig. 2*C* (marked by red box) was further analyzed by EELS mapping (Fig. 2 *D*–*H*), where all of the elements are uniformly distributed in SA-Fe/NG. The overlay signals of Fe and N (Fig. 2*G*) clearly reveal uniform distribution of Fe and N atoms, suggesting that the Fe is surrounded by N. To confirm the universality of Fe atom uniform dispersion in SA-Fe/NG, we selected another region to analyze and found that it still shows a similar uniform dispersion (*SI Appendix*, Fig. S9), as expected.

The X-ray absorption near-edge structure (XANES) and extended X-ray absorption fine structure (EXAFS) were used to explore metal coordination environment and reveal the presence of Fe-N-C configuration in SA-Fe/NG. The XANES curves show that the iron in SA-Fe/NG is more positively charged, compared with Fe foil and Fe/NG, because a shift to the high energy between 7,110 and 7,125 eV was observed in the spectra of Fig. 2*I*. As shown in Fig. 2*J*, EXAFS curve of SA-Fe/NG exhibits an obvious peak at about 1.5 Å, which is attributed to the isolated Fe-N (O) bonds, while Fe/NG is dominated by the peak of Fe-Fe bond at about 2.2 Å (*SI Appendix*, Fig. S10), implying that most iron atoms in SA-Fe/NG form Fe-N (O) moieties. Moreover, the oscillation curves determined by intrinsic atomic arrangements for SA-Fe/NG and Fe/NG are inconsistent (*SI Appendix*, Fig. S11), which confirms that the atomic coordination of the two samples is obviously different. The quantitative analysis of the EXAFS data using the IFEFFIT package (*SI Appendix*, Fig. S12 and Table S3) indicates that the coordination number N of the SA-Fe/NG is 4.0 with the R factor of 0.00457. The fitting results are listed in *SI Appendix*, Table S3.

To gain insight into the Fe coordination type (Fe-N or Fe-O) in the SA-Fe/NG, the Mössbauer spectrum based on the recoil-free absorption of γ-rays by ^{57}Fe nuclei was performed at 295 K (Fig. 2*K*). The Mössbauer curves of SA-Fe/NG were fitted with three doublets (D1, D2, and D3), which are all attributed to Fe-N_x moieties (16). No sextets and singlet were found in Mössbauer curves of SA-Fe/NG, meaning no presence of zero-valence iron crystalline and iron carbide phases in SA-Fe/NG, which is in excellent agreement with the EXAFS and HAADF-STEM results. The main difference between these three type sites is their local coordination environment, i.e., ferrous low-spin Fe-N sites (D1), two ferrous midspin Pc-type Fe-N (D2), and Porph-type Fe-N (D3), in which the proportion of D2 is the largest (*SI Appendix*, Table S4), suggesting that the most coordination types of iron and nitrogen in SA-Fe/NG are the analog of iron phthalocyanine structure. The combination of the Mössbauer spectra and EXAFS analysis definitely verifies the formation of Fe-N_4 moieties in SA-Fe/NG.

Fig. 3*A* presents the ORR polarization curves of two as-synthesized samples in 0.5 M H_2SO_4 and 20% Pt/C in 0.1 M $HClO_4$ using rotating ring-disk electrode (RRDE) test (also see *SI Appendix*, Fig. S13). The SA-Fe/NG shows an onset potential of 0.9 V [versus reversible hydrogen electrode (RHE)] and a half-wave potential of 0.8 V (versus RHE), which is obviously better than Fe/NG and among the rank of excellent nonnoble metal catalysts (*SI Appendix*, Table S5) (5, 28, 34–43). Obviously, the Fe-N_4 moieties in SA-Fe/NG are more efficient than Fe cluster in Fe/NG for ORR in acidic medium. However, the half-wave potential of SA-Fe/NG is still slightly lower (∼30 mV) than 20% Pt/C in 0.1 M $HClO_4$ (0.83 V versus RHE) (Fig. 3*A*).

The kinetic current densities (J_k) of the SA-Fe/NG is 15.6 mA/cm^2 at 0.75 V in acidic media, which is almost the same as that of Pt/C while it is 2.1 times of Fe/NG (*SI Appendix*, Fig. S14). The SA-Fe/NG also displays a small Tafel slope (77 mV/dec) in acidic media (Fig. 3*B*), which is better than 20% Pt/C (104 mV/dec) and Fe/NG (98 mV/dec), indicating that the SA-Fe/NG possesses a fast electron transfer rate. The electron transfer number (n) of SA-Fe/NG is 3.95 at 0.6 V, which was obtained by the Koutecky–Levich (K-L) equation based on the RDE curves from 400 ∼ 2,025 rpm (AFMSRCE rotor; Pine Research Instrumentation) (*SI Appendix*, Fig. S13*B*). Moreover, the n of SA-Fe/NG obtained by RRDE results is about 3.94 in the range of 0.5 ∼ 0.8 V (*SI*

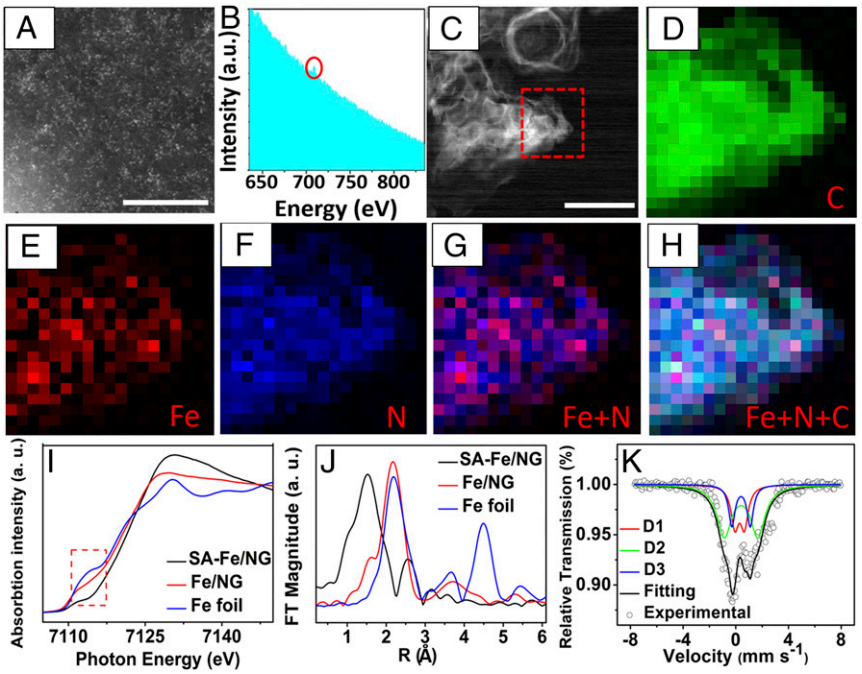

Fig. 2. The structure characterizations of SA-Fe/NG at atomic scales. (*A*) HAADF STEM image of the SA-Fe/NG with iron atom bright points. (Scale bar, 5 nm.) (*B*) EELS atomic spectra of Fe element from the bright points, where the Fe was designated by red circle. (*C*) TEM image of SA-Fe/NG; the red box area in C was further analyzed by EELS mapping with 4× magnification in *D*–*H*. (Scale bar, 200 nm.) (*D*–*H*) EELS mapping of carbon, iron, nitrogen, and superimposed iron and nitrogen and superimposed iron, nitrogen, and carbon for SA-Fe/NG sample. (*I*) XANES spectra and (*J*) Fourier transforms of Fe K-edge spectra of SA-Fe/NG, Fe/NG, and Fe foil. (*K*) ^{57}Fe Mössbauer spectroscopy of SA-Fe/NG.

Appendix, Fig. S15), which is almost the same as that of 20% Pt/C (3.98–3.99) and matches with the ones from the RDE results mentioned above. Importantly, the percentage of peroxide (HO_2^-) yields of SA-Fe/NG are below 5% in the range of 0.2 ~ 0.6 V in acidic condition (Fig. 3*C*), which is also smaller than Fe/NG (~5.80–7.45%). All these observations illustrate that SA-Fe/NG catalyzes the ORR reaction toward a four-electron pathway in acidic medium.

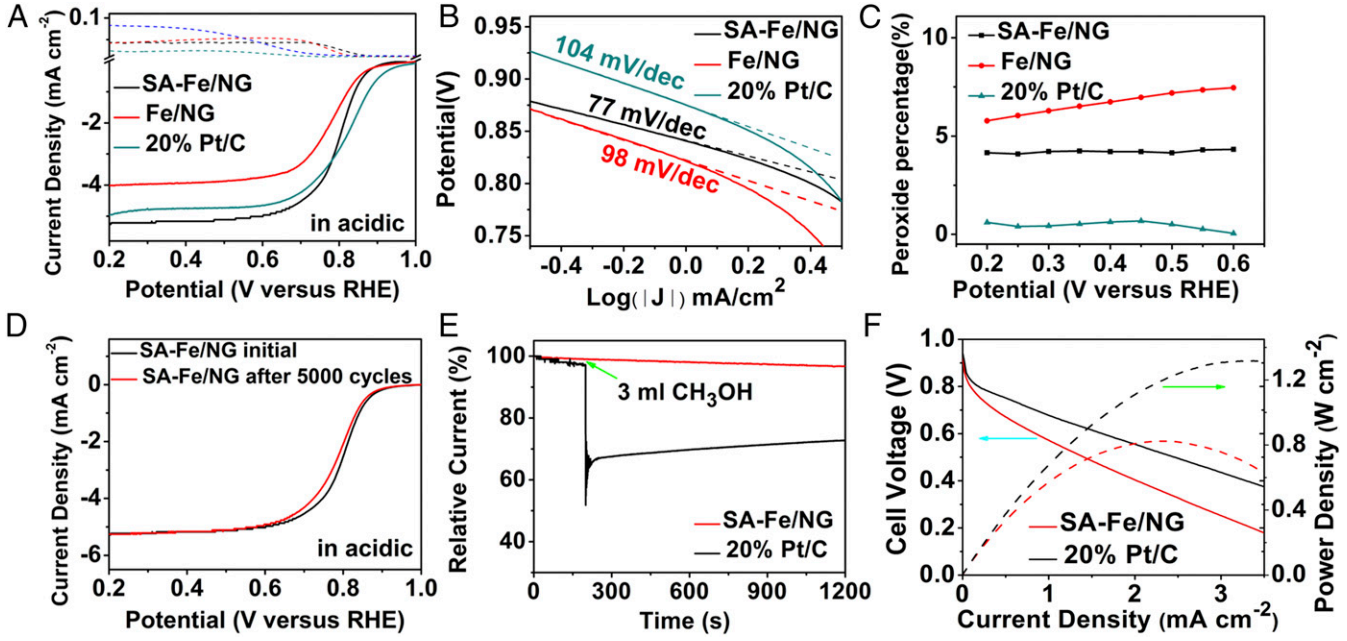

Fig. 3. Characterizations of ORR activity in acidic medium. (*A*) RRDE ORR polarization curves of as-synthesized catalysts in O_2-saturated 0.5 M H_2SO_4 and 20% Pt/C in 0.1 M $HClO_4$ with a sweep rate of 5 mV/s. (*B*) Tafel plots derived from SA-Fe/NG, Fe/NG, and 20% Pt/C in acidic conditions. (*C*) The percentage proportion of peroxide to the total oxygen reduction products of SA-Fe/NG, Fe/NG, and 20% Pt/C at different potentials (0.2–0.6 V) in O_2-saturated acidic solutions from RRDE. (*D*) LSV curves of SA-Fe/NG and before and after 5,000 potential cycles in O_2-saturated 0.5 M H_2SO_4. (*E*) Methanol resistance of SA-Fe/NG in O_2-saturated 0.5 M H_2SO_4 without and with CH_3OH. (*F*) Polarization and power density curves of the SA-Fe/NG-based and 20% Pt/C-based membrane electrode assemblies in PEMFCs. Test conditions: cathode loading 2.0 mg cm^{-2} for SA-Fe/NG and 0.2 mg Pt cm^{-2} for 20% Pt/C, anode loading 0.2 mg Pt cm^{-2}, Nafion 211 membrane, 5-cm^2 electrode area, 80 °C, 100% relative humidity, 2.5-bar O_2/H_2.

The cycling durability tests of SA-Fe/NG and 20% Pt/C catalysts were performed at scanning speed of 1,600 rpm from 0 to 1 V (versus RHE) at scan rate of 50 mV s^{-1}, rotation rate of 1,600 rpm in O_2-saturated acidic solutions (AFMSRCE rotor; Pine Research Instrumentation). Interestingly, the SA-Fe/NG shows more superior stability (~8-mV negative shift for half-wave potential, Fig. 3*D*) than 20% Pt/C (~38-mV negative shift for half-wave potential, *SI Appendix*, Fig. S16) after 5,000 cycles in acidic medium. Methanol tolerance was investigated by instantaneously adding 0.3 mL 2 M methanol in acidic medium (Fig. 3*E*). After adding methanol, almost no oscillation was observed in SA-Fe/NG system, while it decreases about 30% for 20% Pt/C in the same condition.

The excellent ORR activity of SA-Fe/NG in acidic condition was further confirmed by the H_2-O_2 PEMFC measurements. Fig. 3*F* shows the polarization curve and power density plot of PEMFC using SA-Fe/NG as cathode catalyst and Pt/C (20%) as anode catalyst. The SA-Fe/NG catalyst produces a current density of 0.85 A cm^{-2} at 0.6 V, and 3.34 A cm^{-2} at 0.2 V. The maximum power density of the SA-Fe/NG-based PEMFC reaches 823 mW cm^{-2}, which indicates that SA-Fe/NG is among the rank of excellent PGM-free catalysts (*SI Appendix*, Table S6). The excellent performance of the PEMFC may be attributed to the easily accessible dense active sites dispersed on nitrogen-doped carbon nanosheets. The stability test of SA-Fe/NG catalyst was also performed in the PEMFC at 0.5 V with H_2/O_2 feeding (*SI Appendix*, Fig. S17). It shows a typical decay behavior of highly active Fe-N-C catalysts, i.e., a fast decay in the initial stage followed by a stabilized current density ~0.25 A cm^{-2} (44).

SA-Fe/NG possesses not only the excellent ORR performance in acidic condition, but also the extremely better ORR activity in alkaline medium, as expected. The half-wave potential of SA-Fe/NG reaches 0.88 V (versus RHE), which is 30 mV superior to 20% Pt/C (0.85 V, versus RHE) and 62 mV better than Fe/NG in O_2-saturated 0.1 M KOH electrolyte (Fig. 4*A*). Definitely, the Fe-N_4 moieties in SA-Fe/NG significantly improve its ORR performance in alkaline medium. Interestingly, SA-Fe/NG also exhibits an extremely high J_k of 52.4 mA/cm^2 at 0.8 V (Fig. 4*B*), which is 2.8 and 5.7 times of these of 20% Pt/C (18.7 mA/cm^2) and Fe/NG (9.14 mA/cm^2), respectively.

The excellent ORR activity of SA-Fe/NG was also confirmed by Tafel slope. SA-Fe/NG shows a smaller Tafel slope (82 mV/dec) than Fe/NG (85 mV/dec) and 20% Pt/C (89 mV/dec) in 0.1 M KOH (*SI Appendix*, Fig. S18). This means that the rate-determining step is the last electron-transfer step in ORR process of SA-Fe/NG, which is similar to 20% Pt/C. The ORR kinetics of SA-Fe/NG was also studied by an RDE system at different rotating rates in 0.1 M KOH (*SI Appendix*, Fig. S19). The K-L equation calculated *n* value of SA-Fe/NG is 3.87–3.96 in the range of 0.5 ~ 0.8 V based on the RDE curves (*SI Appendix*, Fig. S19*B*). The RRDE test reveals that the HO_2^- yields of SA-Fe/NG in alkaline condition are below 8.6% in the range of 0.2–0.6 V, which is almost similar to 20% Pt/C (*SI Appendix*, Fig. S20). The *n* of SA-Fe/NG obtained by RRDE results is 3.83–3.97 in the scanning range of potential (*SI Appendix*, Fig. S20), which is consistent with the RDE results. Both the *n* and peroxide yields indicate a four-electron pathway of SA-Fe/NG for ORR in alkaline conditions.

The stability and antimenthol of the samples were also tested. As expected, the half-wave potential of SA-Fe/NG presents only negative shift of 9 mV after 5,000 cycles in alkaline solution, which is more stability than 20% Pt/C (~37-mV negative shift for half-wave potential), as shown in *SI Appendix*, Fig. S21. Moreover, all of the chronoamperometry tests and cyclic voltammetry and linear sweep voltammetry (LSV) curves (*SI Appendix*, Figs. S22 and S23) indicate that the SA-Fe/NG possesses the extremely stable methanol resistance in alkaline medium.

To evaluate the possible application of SA-Fe/NG, a home-made Zn-air battery was assembled (*SI Appendix*, Fig. S24). For comparison, the counterpart with 20% Pt/C as air cathode was also made. The polarization curves display that the discharging voltage of the SA-Fe/NG-based Zn-air battery is more positive than the Pt/C-based battery in the same mass loading of catalyst. SA-Fe/NG–based battery shows a current density of ~60 mA/cm^2 at 1.0 V while it is ~45 mA/cm^2 at 1.0 V for the 20% Pt/C-based one (Fig. 4*C*). The power density peak of SA-Fe/NG–based battery reaches 91 mW/cm^2 at 186 mA/cm^2, about 1.08 times the 20% Pt/C-based one (84 mW/cm^2 at 164 mA/cm^2). This indicates that the SA-Fe/NG catalyst possesses the highly active sites for ORR, and the porous electrode prepared from the SA-Fe/NG catalyst is beneficial for efficient mass transport O_2, which contributes to the excellent performance of SA-Fe/NG–based battery. To evaluate the stability of SA-Fe/NG, a rechargeable Zn-air battery was assembled. The mixture of SA-Fe/NG and IrO_2 was used as an air catalyst and the coupled 20% Pt/C IrO_2 severed as a counterpart. (Fig. 4*D*). The SA-Fe/NG–based battery produces the discharging potential of 1.24 V and charging potential of 1.97 V at 10 mA/cm^2. As expected, the discharging potential of SA-Fe/NG–based battery does not exhibit significant change after 20 h charging/discharging cycle tests (~30 cycles), whereas the overpotential (the difference between charging and discharging potentials) of 20% Pt/C-IrO_2 increases to 0.81 V from the initial 0.72 V, which demonstrates the superior durability of the SA-Fe/NG–based battery. Moreover, the morphology of SA-Fe/NG was well preserved after a long stability test for Zn-air battery (*SI Appendix*, Fig. S25).

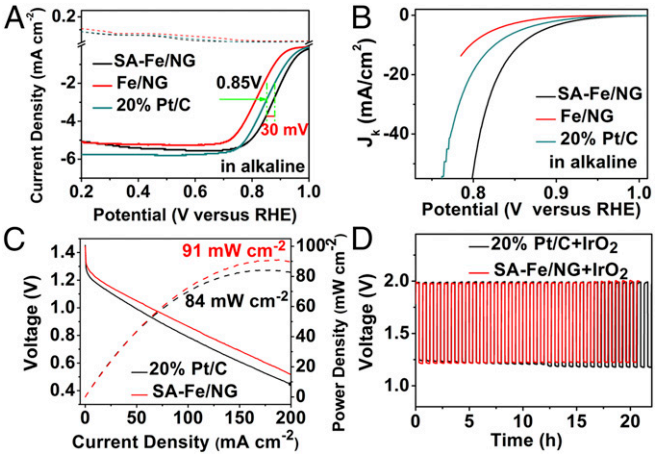

Fig. 4. Characterizations of ORR activity in alkaline medium. (*A*) RRDE ORR polarization curves of SA-Fe/NG, Fe/NG, and 20% Pt/C with a sweep rate of 5 mV/s and electrode-rotation speed of 1,600 rpm in O_2-saturated 0.1 M KOH (AFMSRCE rotor; Pine Research Instrumentation). (*B*) Kinetic current density of SA-Fe/NG, Fe/NG, and 20% Pt/C in O_2-saturated 0.1 M KOH. (*C*) Discharging polarization curves and the corresponding power plots of SA-Fe/NG–based and 20% Pt/C-based batteries. (*D*) Cycling performance at the charging and discharging current density of 10 mA cm^{-2} of SA-Fe/NG+IrO_2–based and 20% Pt/C+IrO_2-based batteries.

Recent experiments have verified that the Fe-N_x species in SACs is more efficient for ORR. However, all previous studies did not unveil the origin of high-ORR activity of SACs, and one cannot identify that the active sites are from the Fe-pyridinic-N or Fe-pyrrolic-N moieties (11, 20, 33). To reveal the origin of high-ORR activity of SA-Fe/NG, on the basis of the experiments, two models of Fe@pyridine-N and Fe@pyrrole-N with Fe-N_4 coordination were proposed. For both models, we considered Fe atom and C atom next to N atom as possible active sites for ORR, namely (*i*) Fe@pyridinic N(Fe), (*ii*) Fe@pyridinic N(C), (*iii*) Fe@pyrrolic N(Fe), and (*iv*) Fe@pyrrolic N(C) (*SI Appendix*, Fig. S26).

According to electrochemical framework developed by Nørskov et al. (45) (calculation details were presented in *SI Appendix*, Figs S27 and S28 and Tables S7–S9), we first investigated the electrochemical properties of Pt (111), which is commonly considered as a theoretical model of commercial Pt/C, and calculated the free-energy diagrams of the four-electron transfer ORR on Pt(111) in alkaline condition (*SI Appendix*, Fig. S29*A*). When the output potential (U_{RHE}) increases from 0 to 0.80 V, the free energy of the last electron transfer step in the reaction becomes zero first while the other steps remain downhill, which indicates

that the four-electron transfer ORR cannot proceed spontaneously at $U_{RHE} > 0.80$ V since the last step become endothermic ($\Delta G > 0$). Therefore, $U_{RHE} = 0.80$ V is the onset potential ($U^{onset}{}_{RHE}$) of Pt (111), which is in agreement with previous theoretical works (45). The free-energy paths of four-electron transfer ORR on Fe@pyridinic N(Fe), Fe@pyrrolic N(Fe), and Fe@pyrrolic N(C) at $U_{RHE} = 0$ V are shown in *SI Appendix*, Fig. S29*B*. $U^{onset}{}_{RHE}$ and ΔG_{max} of these catalyst models can be obtained from *SI Appendix*, Fig. S29*B* and Table S10. To understand the selectivity of ORR catalysts, it is necessary to explore the competition between the main reaction (i.e., four-electron transfer ORR toward H_2O) and the side reaction (i.e., two-electron transfer ORR toward H_2O_2). The free-energy diagram of four-electron transfer ORR and the two-electron transfer ORR at $U_{RHE} = 0.6$ V is plotted in *SI Appendix*, Fig. S30. ΔG_{H2O} and ΔG_{H2O2} are reaction free energy of potential-determining steps of four-electron transfer ORR and two-electron transfer ORR at $U_{RHE} = 0.6$ V, respectively (*SI Appendix*, Table S11). It is noted that any reaction intermediates (O, OH, and OOH) cannot be adsorbed on Fe@pyridinic N(C) stably and would diffuse to Fe@pyridinic N(Fe), while the intermediates can be adsorbed on Fe@pyrrolic N(C). Therefore, Fe@pyrrolic N(C) may act as active sites for ORR, while Fe@pyridinic N(C) cannot. According to previous theoretical calculations (46–48), the weaker binding strength for Fe@pyridinic N(C) to adsorb reaction intermediates (O, OH, and OOH) is attributed to a lower energy level location of the p band of Fe@pyridinic N(C) than that of Fe@pyrrolic N(C) (*SI Appendix*, Fig. S31).

Fig. 5*A* shows the comparisons of $U^{onset}{}_{RHE}$ of four-electron transfer ORR from experiments and DFT calculations. The theoretical $U^{onset}{}_{RHE}$ of Fe@pyrrolic N(Fe) rather than Fe@pyridinic N(Fe) is higher than that of Pt(111), which satisfactorily agrees with the experimental results, i.e., $U^{onset}{}_{RHE}$ of SA-Fe/NG is higher than 20% Pt/C (Fig. 4*A*). The experimentally measured exchange current densities (j_0^{expt}) of samples can be calculated by Tafel plots (49) (*SI Appendix*, Fig. S18), while they can also be obtained theoretically by the microkinetic model (46, 50, 51). The theoretically calculated j_0 is in direct proportion with $\Delta G_{max}{}^{-1}$. Fig. 5*B* shows that Fe@pyrrolic N(Fe) possesses higher $\Delta G_{max}{}^{-1}$ than Pt(111), meaning that it has a higher j_0 than Pt(111), which agrees qualitatively with the fact that SA-Fe/NG has higher j_0^{expt} than Pt/C (*SI Appendix*, Fig. S18). Moreover, Fe@pyrrolic N(Fe) shows a lower ΔG_{H2O}-ΔG_{H2O2} than Pt(111) (*SI Appendix*, Fig. S20), meaning that H_2O_2% of Fe@pyrrolic N(Fe) is lower than that of Pt(111), which also excellently agrees with the experimental result, i.e., the H_2O_2% of SA-Fe/NG is lower than that of 20% Pt/C (Fig. 5*C*). All above analysis indicates that the calculated electrocatalytic performance ($U^{onset}{}_{RHE}$, ΔG_{max}, and ΔG_{H2O2}) of Fe@pyrrolic-N (Fe) is superior to Pt (111), which coincides with the fact that the ORR performance ($U^{onset}{}_{RHE}$, j_0^{expt}, and H_2O_2%) of SA-Fe/NG is better than 20% Pt/C. By matching the DFT results with experimental data, we believe that the Fe-N_4 moieties in SA-Fe/NG should be the Fe-pyrrolic-N species. Interestingly, besides the high activity of Fe@pyrrolic N(Fe) itself, SA-Fe incorporation also arouses the eight carbon atoms next to the nitrogen atom to become ORR catalytic sites [Fig. 5*D*, Fe@pyrrolic N(C) ORR activity in *SI Appendix*, Table S11], i.e., the synergistic effect of both Fe and C atoms next to pyrrolic-N further improves the catalytic activity of SA-Fe/NG, while the synergistic effect does not occur in the Fe@pyridinic-N species. Combining the DFT calculations with experimental results, we unveiled that the formation of Fe-pyrrolic N moieties is the origin of high-ORR activity of SA-Fe/NG, because an SA-Fe incorporation leads to the increase of active sites in an order of magnitude.

Conclusions

In summary, we have proposed an efficient and universal surfactant-assisted method to successfully synthesize the single-atom iron catalyst (SA-Fe/NG). It is found that the addition of surfactant F127 is the key to synthesizing the SA-Fe/NG catalyst, because it helps disperse the iron to easily form Fe-N_x moieties, and Fe-doped F127 sheets strongly anchor on the g-C_3N_4 substrate so that the surface Fe clusters can be easily removed by acid etching. The SA-Fe/NG exhibited excellent ORR activity, and the onset and half-wave potentials reach 1.0 V (vs. RHE) and 0.88 V

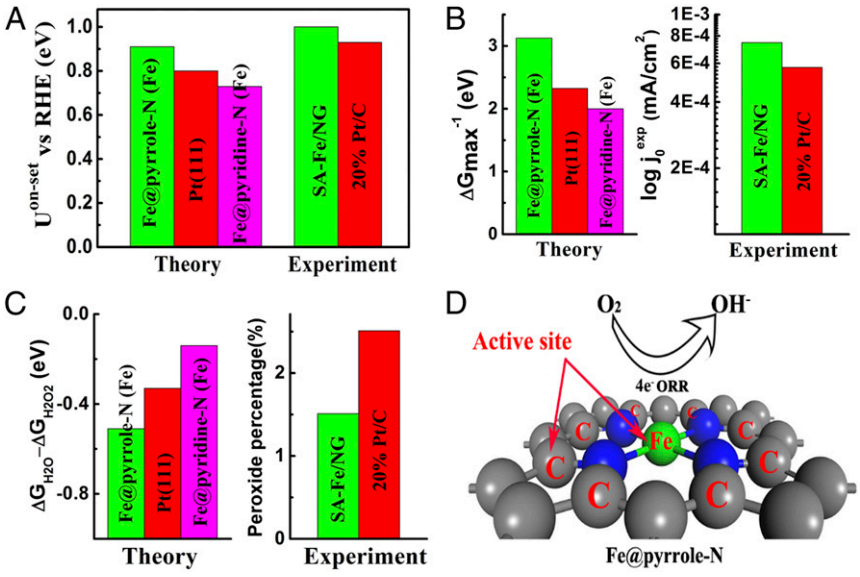

Fig. 5. DFT calculation studies on the origin of high-ORR activity of SA-Fe/NG. (*A*) Comparison of onset potential with RHE ($U^{onset}{}_{RHE}$) between theoretical calculation and experiment measurement for four-electron transfer ORR on different catalysts in an alkaline electrolyte. (*B*) Comparison between the theoretical reaction free energy of potential-determining step at equilibrium potential (ΔG_{max}) and the exchange current density in experiment (j_0^{exp}) for four-electron transfer ORR on different catalysts in an alkaline electrolyte. (*C*) The difference between the theoretical reaction free energy of potential-determining step for four-electron and two-electron transfer ORR (ΔG_{H2O}-ΔG_{H2O2}), and the experimental peroxide percentage at $U_{RHE} = 0.6$ V on different catalysts in an alkaline electrolyte. (*D*) Computational models of Fe@pyrrolic N moieties for ORR, where both Fe atom and eight-carbon atoms next to pyrrolic N are the active sites marked by red letters.

in alkaline medium while they are 0.9 V (vs. RHE) and 0.8 V in acidic medium, respectively. Moreover, SA-Fe/NG possesses extremely long-term stability and tolerance to methanol. The outstanding ORR performance of SA-Fe/NG in acidic and alkaline media was attributed to the Fe-N_4 moieties. Combining the experimental data and DFT results, we further revealed that the formation of Fe-pyrrolic-N moieties is the origin of high-ORR activity of SA-Fe/NG, because an SA-Fe incorporation creates an Fe atom and eight C atom active sites next to pyrrolic N, leading to the increase of active sites in an order of magnitude. Interestingly, the SA-Fe/NG–based PEMFC and Zn-air battery also show excellent performance, large power density, and good stability, meaning the grand perspective of SA-Fe/NG for practical applications. In short, the efficient and universal surfactant-assisted method can be easily extended to synthesis of other SACs, and the exposure of the origin of high-ORR activity of SA-Fe/NG will open an avenue for developing highly efficient heterogeneous catalysts for energy storage and conversion.

Methods

Experimental details on synthesis and characterization of SA-Fe/NG catalyst, including structure and electrochemical characterization, and the SA-Fe/NG–based PEMFC and Zn-air battery measurements, and DFT calculation details on models, reaction mechanism, and reaction free energy, are provided in *SI Appendix*.

ACKNOWLEDGMENTS. This work is supported by National Science Fund for Distinguished Young Scholars (Grant 21625601) and the Major Project of NSF of China (Grants 91334203, 91634116, and 21576008).

1. Debe MK (2012) Electrocatalyst approaches and challenges for automotive fuel cells. *Nature* 486:43–51.
2. Jaouen F, Lefèvre M, Dodelet JP, Cai M (2006) Heat-treated Fe/N/C catalysts for O_2 electroreduction: Are active sites hosted in micropores? *J Phys Chem B* 110:5553–5558.
3. Wu G, Zelenay P (2013) Nanostructured nonprecious metal catalysts for oxygen reduction reaction. *Acc Chem Res* 46:1878–1889.
4. Wang X, et al. (2016) Directly converting Fe-doped metal–organic frameworks into highly active and stable Fe-N-C catalysts for oxygen reduction in acid. *Nano Energy* 25: 110–119.
5. Li Q, et al. (2016) High-performance direct methanol fuel cells with precious-metal-free cathode. *Adv Sci (Weinh)* 3:1600140.
6. Zitolo A, et al. (2015) Identification of catalytic sites for oxygen reduction in iron- and nitrogen-doped graphene materials. *Nat Mater* 14:937–942.
7. Xiang Z, et al. (2014) Highly efficient electrocatalysts for oxygen reduction based on 2D covalent organic polymers complexed with non-precious metals. *Angew Chem Int Ed Engl* 53:2433–2437.
8. Wu G, et al. (2016) Carbon nanocomposite catalysts for oxygen reduction and evolution reactions: From nitrogen doping to transition-metal addition. *Nano Energy* 29: 83–110.
9. Ramaswamy N, Tylus U, Jia Q, Mukerjee S (2013) Activity descriptor identification for oxygen reduction on nonprecious electrocatalysts: Linking surface science to coordination chemistry. *J Am Chem Soc* 135:15443–15449.
10. Wu G, More KL, Johnston CM, Zelenay P (2011) High-performance electrocatalysts for oxygen reduction derived from polyaniline, iron, and cobalt. *Science* 332:443–447.
11. Zhu C, Fu S, Shi Q, Du D, Lin Y (2017) Single-atom electrocatalysts. *Angew Chem Int Ed Engl* 56:13944–13960.
12. Zhang H, et al. (2017) Single atomic iron catalysts for oxygen reduction in acidic media: Particle sicne control and thermal activation. *J Am Chem Soc* 139: 14143–14149.
13. Deng D, et al. (2015) A single iron site confined in a graphene matrix for the catalytic oxidation of benzene at room temperature. *Sci Adv* 1:e1500462.
14. Zhang H, et al. (2016) Efficient visible-light-driven carbon dioxide reduction by a single-atom implanted metal organic framework. *Angew Chem Int Ed Engl* 55: 14310–14314.
15. Yang XF, et al. (2013) Single-atom catalysts: A new frontier in heterogeneous catalysis. *Acc Chem Res* 46:1740–1748.
16. Kramm UI, et al. (2016) On an easy way to prepare metal–nitrogen doped carbon with exclusive presence of MeN_4-type sites active for the ORR. *J Am Chem Soc* 138:635–640.
17. Zhang H, Liu G, Shi L, Ye J (2017) Single-atom catalysts: Emerging multifunctional materials in heterogeneous catalysis. *Adv Energy Mater* 8:1701343.
18. Yin P, et al. (2016) Single cobalt atoms with precise N-coordination as superior oxygen reduction reaction catalysts. *Angew Chem Int Ed Engl* 55:10800–10805.
19. Chen P, et al. (2017) Atomically dispersed iron-nitrogen species as electrocatalysts for bifunctional oxygen evolution and reduction reactions. *Angew Chem Int Ed Engl* 56: 610–614.
20. Chen Y, et al. (2017) Isolated single iron atoms anchored on N-doped porous carbon as an efficient electrocatalyst for the oxygen reduction reaction. *Angew Chem Int Ed Engl* 56:6937–6941.
21. Zhang T, et al. (2016) Single-atom dispersed Co-N-C catalyst: Structure identification and performance for hydrogenative coupling of nitroarenes. *Chem Sci (Camb)* 7: 5758–5764.
22. Zheng Y, et al. (2017) Molecule-level g-C_3N_4 coordinated transition metals as a new class of electrocatalysts for oxygen electrode reactions. *J Am Chem Soc* 139: 3336–3339.
23. Lai Q, et al. (2017) Metal–organic-framework-derived Fe-N/C electrocatalyst with five-coordinated Fe-Nx sites for advanced oxygen reduction in acid media. *ACS Catal* 7: 1655–1663.
24. Han Y, et al. (2017) Hollow N-doped carbon spheres with isolated cobalt single atomic sites: Superior electrocatalysts for oxygen reduction. *J Am Chem Soc* 139: 17269–17272.
25. Chung HT, et al. (2017) Direct atomic-level insight into the active sites of a high-performance PGM-free ORR catalyst. *Science* 357:479–484.
26. Fei H, et al. (2018) General synthesis and definitive structural identification of MN_4C_4 single-atom catalysts with tunable electrocatalytic activities. *Nat Catal* 1:63–72.
27. Zitolo A, et al. (2017) Identification of catalytic sites in cobalt-nitrogen-carbon materials for the oxygen reduction reaction. *Nat Commun* 8:957.
28. Strickland K, et al. (2015) Highly active oxygen reduction non-platinum group metal electrocatalyst without direct metal-nitrogen coordination. *Nat Commun* 6:7343.
29. Zhu C, et al. (2017) Self-assembled Fe-N-doped carbon nanotube aerogels with single-atom catalyst feature as high-efficiency oxygen reduction electrocatalysts. *Small* 13: 1603407.
30. Wang B, et al. (2017) Simple-cubic carbon frameworks with atomically dispersed iron dopants toward high-efficiency oxygen reduction. *Nano Lett* 17:2003–2009.
31. Gupta A, Kumar A, Waghmare UV, Hegde MS (2009) Origin of activation of lattice oxygen and synergistic interaction in bimetal-ionic $Ce_{0.89}Fe_{0.1}Pd_{0.01}O_2{-}\delta$ catalyst. *Chem Mater* 21:4880–4891.
32. Kundu S, et al. (2009) Electrocatalytic activity and stability of nitrogen-containing carbon nanotubes in the oxygen reduction reaction. *J Phys Chem C* 113:14302–14310.
33. Shen H, et al. (2017) Atomically FeN_2 moieties dispersed on mesoporous carbon: A new atomic catalyst for efficient oxygen reduction catalysis. *Nano Energy* 35:9–16.
34. Lin L, Zhu Q, Xu AW (2014) Noble-metal-free Fe-N/C catalyst for highly efficient oxygen reduction reaction under both alkaline and acidic conditions. *J Am Chem Soc* 136:11027–11033.
35. Zhao D, et al. (2012) Iron imidazolate framework as precursor for electrocatalysts in polymer electrolyte membrane fuel cells. *Chem Sci (Camb)* 3:3200–3205.
36. Hu Y, et al. (2014) Hollow spheres of iron carbide nanoparticles encased in graphitic layers as oxygen reduction catalysts. *Angew Chem Int Ed Engl* 53:3675–3679.
37. Yasuda S, Furuya A, Uchibori Y, Kim J, Murakoshi K (2016) Iron–nitrogen-doped vertically aligned carbon nanotube electrocatalyst for the oxygen reduction reaction. *Adv Funct Mater* 26:738–744.
38. Lin Q, et al. (2015) Heterometal-embedded organic conjugate frameworks from alternating monomeric iron and cobalt metalloporphyrins and their application in design of porous carbon catalysts. *Adv Mater* 27:3431–3436.
39. Xiao M, Zhu J, Feng L, Liu C, Xing W (2015) Meso/macroporous nitrogen-doped carbon architectures with iron carbide encapsulated in graphitic layers as an efficient and robust catalyst for the oxygen reduction reaction in both acidic and alkaline solutions. *Adv Mater* 27:2521–2527.
40. Wang Y, Kong A, Chen X, Lin Q, Feng P (2015) Efficient oxygen electroreduction: Hierarchical porous Fe–N-doped hollow carbon nanoshells. *ACS Catal* 5:3887–3893.
41. Wei J, et al. (2015) Nitrogen-doped nanoporous carbon/graphene nano-sandwiches: Synthesis and application for efficient oxygen reduction. *Adv Funct Mater* 25: 5768–5777.
42. Sa YJ, et al. (2016) A general approach to preferential formation of active Fe-N_x sites in Fe-N/C electrocatalysts for efficient oxygen reduction reaction. *J Am Chem Soc* 138: 15046–15056.
43. Wang Q, et al. (2014) Phenylenediamine-based $FeN_{(x)}$/C catalyst with high activity for oxygen reduction in acid medium and its active-site probing. *J Am Chem Soc* 136: 10882–10885.
44. Chenitz R, et al. (2018) A specific demetalation of Fe-N_4 catalytic sites in the micropores of NC-Ar+NH_3 is at the origin of the initial activity loss of this highly active Fe/N/C catalyst used for the reduction of oxygen in PEM fuel cell. *Energy Environ Sci* 11: 365–382.
45. Nørskov JK, et al. (2004) Origin of the overpotential for oxygen reduction at a fuel-cell cathode. *J Phys Chem B* 108:17886–17892.
46. Jiao Y, Zheng Y, Davey K, Qiao S (2016) Activity origin and catalyst design principles for electrocatalytic hydrogen evolution on heteroatom-doped graphene. *Nat Energy* 1:16130–16138.
47. Zheng Y, Jiao Y, Jaroniec M, Qiao SZ (2015) Advancing the electrochemistry of the hydrogen-evolution reaction through combining experiment and theory. *Angew Chem Int Ed Engl* 54:52–65.
48. Jiao Y, Zheng Y, Jaroniec M, Qiao SZ (2015) Design of electrocatalysts for oxygen- and hydrogen-involving energy conversion reactions. *Chem Soc Rev* 44:2060–2086.
49. Bard A, Faulkner L (1980) *Electrochemical Methods: Fundamentals and Applications* (Wiley, New York), pp 669–676.
50. Zheng Y, et al. (2014) Toward design of synergistically active carbon-based catalysts for electrocatalytic hydrogen evolution. *ACS Nano* 8:5290–5296.
51. Jiao Y, Zheng Y, Jaroniec M, Qiao SZ (2014) Origin of the electrocatalytic oxygen reduction activity of graphene-based catalysts: A roadmap to achieve the best performance. *J Am Chem Soc* 136:4394–4403.